Earthquake Geotechnical Engineering for Protection and Development of Environment and Constructions – Silvestri & Moraci (Eds)
© 2019 Associazione Geotecnica Italiana, Rome, Italy, ISBN 978-0-367-14328-2

Numerical modelling of underground tunnel in rock under seismic loading with polygonal finite elements

T. Saksala
Laboratory of Civil Engineering, Tampere University of Technology, Tampere, Finland

ABSTRACT: This paper deals with numerical modelling of rock failure around an underground tunnel under remote seismic loading. A continuum based numerical model consisting of a vis-codamage-viscoplastic material model for rock and a polygonal finite elements scheme to model the wave propagation in rock is presented. The numerical simulations of an underground opening under a compressive stress wave demonstrate that this approach, despite the limitations of the continuum approach in modelling rock fracture, predict many important features of the rockburst (ejection) into the tunnel in computation times fractional to those of the particle methods.

1 INTRODUCTION

Numerical modelling of rockbursting in underground tunnels due to remote seismic event is an important task in geotechnical engineering. A model with predictive capabilities provides a valuable tool, e.g. for the design of the rock support systems based on rockbolting (Brady & Brown, 1993; Li, 2017). Modern computers enable full-blown simulations of fracture processes in geostructures under complex dynamic loadings. Numerical modelling reduces substantially the experimentation costs and increases the understanding of the failure processes under dynamic loading. The two major approaches for numerical modelling in geomechanics are the finite element method (FEM) and the discrete element method (DEM). Due to the underlying discontinuum assumption, DEM is naturally more suitable for modelling problems such as rockbursts in underground tunnel walls during seismic events, see Raffaldi & Loken (2016). However, FEM can provide vital information on the tunnel stability under seismic loading in computation times drastically shorter than those with DEM, see Wen et al. (2017).

This paper deals with numerical modelling of rockbursts in an underground tunnel under seismic loading. This problem is tackled with a numerical method including a constitutive model for rock and a finite element model for seismic wave propagation simulation. As for the constitutive model, the viscodamage-viscoplasticity model for rock by Saksala (2018) is employed. In this model, the Rankine criterion indicates the tensile stress states leading to rate-dependent anisotropic damage. In compression, a Mohr-Coulomb viscoplasticity model governs the inelastic deformation and compressive strength degradation. The rock around the tunnel is described by polygonal finite elements. The equations of motion are solved with an explicit time marching scheme.

In the numerical examples, 2D analyses of an underground tunnel are presented in order to demonstrate the performance of the method. The seismic loading is specified as a synthetic waveform. Two cases are simulated: First, the tunnel is close to the surface so that the overburden pressure can be neglected while in the second case the tunnel is subjected to a confining pressure simulating a case of deep underground opening.

2 NUMERICAL MODELLING

2.1 *Constitutive model for rock*

The constitutive model for rock is developed within the small deformation framework, which enables the additive decomposition of the strain into elastic, viscoplastic, and viscodamage components, respectively, as

$$\boldsymbol{\varepsilon} = \boldsymbol{\varepsilon}_{\mathrm{e}} + \boldsymbol{\varepsilon}_{\mathrm{vp}} + \boldsymbol{\varepsilon}_{\mathrm{vd}} \tag{1}$$

This decomposition is justified by the brittle nature of rock.

Rocks exhibit both stiffness and strength degradation as well as irreversible strains (Brady & Brown, 1993). Irreversible deformation takes place especially in compression while in tension it can be usually neglected. Therefore, a constitutive model capable of accounting for both damage and plasticity is needed to correctly predict the behavior of rocks. Moreover, microcracks in rock usually display loading induced orientation which results in damage-induced anisotropy. For this reason, an anisotropic damage model is often preferable. Rocks are also strongly strain rate-sensitive materials (Zhang & Zhao, 2014) which should be accounted for in modelling. In the present model, the rate-sensitivity is accommodated by viscosity.

In compression, the viscoplasticity model based on the Mohr-Coulomb (MC) criterion is formulated with the consistency approach by Wang et al. (1997) as

$$\begin{aligned}
&f_{\mathrm{MC}}(\boldsymbol{\sigma}, \lambda_{\mathrm{vp}}, \dot{\lambda}_{\mathrm{vp}}) = \tfrac{k_\varphi - 1}{2}(\sigma_x + \sigma_y) + (k_\varphi + 1)\sqrt{\left(\tfrac{\sigma_x - \sigma_y}{2}\right)^2 + \sigma_{xy}^2} - \sigma_{\mathrm{c}}(\lambda_{\mathrm{MC}}, \dot{\lambda}_{\mathrm{MC}}) \\
&\underline{\varepsilon}_{\mathrm{vp}} = \dot{\lambda}_{\mathrm{MC}} \frac{\partial g_{\mathrm{MC}}}{\partial \boldsymbol{\sigma}}, \quad \sigma_{\mathrm{c}}(\lambda_{\mathrm{MC}}, \dot{\lambda}_{\mathrm{MC}}) = \sigma_{\mathrm{c0}} + h_{\mathrm{MC}}\lambda_{\mathrm{MC}} + s_{\mathrm{MC}}\dot{\lambda}_{\mathrm{MC}} \\
&g_{\mathrm{MC}}(\boldsymbol{\sigma}) = \tfrac{k_\psi - 1}{2}(\sigma_x + \sigma_y) + (k_\psi + 1)\sqrt{\left(\tfrac{\sigma_x - \sigma_y}{2}\right)^2 + \sigma_{xy}^2} \\
&k_\varphi = (1 + \sin\varphi)/(1 - \sin\varphi), \; k_\psi = (1 + \sin\psi)/(1 - \sin\psi) \\
&f_{\mathrm{MC}} \le 0, \quad \dot{\lambda}_{\mathrm{MC}} 0, \quad \dot{\lambda}_{\mathrm{MC}} f_{\mathrm{MC}} = 0
\end{aligned} \tag{2}$$

where the components of the stress $\boldsymbol{\sigma}$ are given in xy-coordinate system, λ_{MC}, λ_{MC} denote the viscoplastic increment and its rate, respectively, σ_{c0} is the compressive strength, h_{MC} and s_{MC} are the softening and viscosity moduli in compression, g_{MC} is the plastic potential defined with the dilation angle ψ, instead of the friction angle φ. The amount of softening is calibrated by model II fracture energy: $h_{\mathrm{MC}} = -\sigma_{\mathrm{c0}}{}^2 l_e / 2G_{\mathrm{IIc}}$ with l_e being a characteristic length of a finite element. Finally, the last equations in (2) are the Kuhn-Tucker type of consistency conditions.

In tension, the Rankine criterion based viscodamage consistency model governs the softening and anisotropic stiffness degradation. This model, given in the compliance damage format, is defined as

$$\begin{aligned}
&f_{\mathrm{R}}(\boldsymbol{\sigma}, \lambda_{\mathrm{R}}, \dot{\lambda}_{\mathrm{R}}) = \underbrace{\tfrac{1}{2}(\sigma_x + \sigma_y) + \sqrt{\left(\tfrac{\sigma_x - \sigma_y}{2}\right)^2 + \sigma_{xy}^2}}_{\hat{f}_{\mathrm{R}}(\sigma)} - \sigma_{\mathrm{t}}(\lambda_{\mathrm{R}}, \dot{\lambda}_{\mathrm{R}}) \\
&\dot{\mathbf{D}} = \frac{\dot{\lambda}_{\mathrm{R}}}{\hat{f}_{\mathrm{R}}(\boldsymbol{\sigma})} \frac{\partial f_{\mathrm{R}}}{\partial \boldsymbol{\sigma}} \otimes \frac{\partial f_{\mathrm{R}}}{\partial \boldsymbol{\sigma}} \\
&\sigma_{\mathrm{t}}(\lambda_{\mathrm{R}}, \dot{\lambda}_{\mathrm{R}}) = \sigma_{\mathrm{t0}} + h_{\mathrm{R}}\lambda_{\mathrm{R}} + s_{\mathrm{R}}\dot{\lambda}_{\mathrm{R}}, \quad h_{\mathrm{R}} = -g\sigma_{\mathrm{t0}} \exp(-g\kappa_{\mathrm{R}}) \\
&f_{\mathrm{R}} \le 0, \quad \dot{\lambda}_{\mathrm{R}} 0, \quad \dot{\lambda}_{\mathrm{R}} f_{\mathrm{R}} = 0
\end{aligned} \tag{3}$$

where σ_{t0} is the tensile strength, $\mathbf{D}$ is the (fourth order) compliance tensor, whereas the meanings of the rest of symbols are equivalent to the corresponding ones related to the

viscoplastic model. The softening in tension is exponential and it is controlled by mode I fracture energy through $g = \sigma_{t0} l_e / G_{Ic}$.

In the present compliance damage format, the current value of compliance tensor, which evolves by damage from the initial value $\mathbf{D}_{(t=0)} = \mathbf{0}$, is added to the elastic compliance to obtain: $\mathbf{E}_d = (\mathbf{C}_e + \mathbf{D})^{-1}$ with $\mathbf{E}_d$ and $\mathbf{C}_e$ being the damaged stiffness and the standard elasticity tensor, respectively. Finally, the relation between the damage compliance and the damage deformation reads $\boldsymbol{\varepsilon}_d = \mathbf{D}:\boldsymbol{\sigma}$.

The stress return mapping with this combined viscodamage-viscoplastic consistency model can be performed with the standard methods of multisurface plasticity (i.e. the elastic predictor-plastic corrector split) due to the fact the consistency is enforced in both of the components, see Saksala (2018) for details.

2.2 *Polygonal finite elements*

Polygonal finite elements have resurfaced into the focus of research. Compared to the usual triangular and quadrilateral elements, they offer, in many cases, greater flexibility in meshing arbitrary geometries, better accuracy in the numerical solution, better description of certain materials, and less locking-prone behavior under volume-preserving deformation (Sukumar & Tabarraei, 2004). Saksala (2018) applied the polygonal finite elements in numerical modelling of heterogeneous rocks with good results.

The present finite element formulation is based on the Wachspress interpolation functions implemented in Matlab by Talischi et al. (2012b). The standard isoparametric mapping from a reference element to the physical element, as illustrated in Figure 1, is used here as well.

The mathematical expression for a barycentric Wachspress shape function at node i of a reference n-gon reads

$$N_i(\xi) = \frac{\alpha_i(\xi)}{\sum_{j=1}^{n} \alpha_j(\xi)}, \quad \alpha_i(\xi) = \frac{A(\mathbf{p}_{i-1}, \mathbf{p}_i, \mathbf{p}_{i+1})}{A(\mathbf{p}_{i-1}, \mathbf{p}_i, \xi) A(\mathbf{p}_i, \mathbf{p}_{i+1}, \xi)} \tag{4}$$

where $A(a, b, c)$ denotes the signed area of triangle a, b, c (Figure 1a). The numerical integration scheme is based on a sub-division of the reference polygon into triangles and applying a three-point quadrature for each triangle (resulting $3n$ integration points for each n-gon), as illustrated in Figure 1b. The polygonal finite element mesh is generated by the PolyMesher code developed by Talischi et al. (2012a). This code generates 2D Voronoi diagrams (tessellations) consisting of centroidal (or alternatively non-centroidal) Voronoi cells.

Since strain rate effects of rock are considered, the governing equations of motion are solved with an explicit time integrator. The explicit modified Euler method (Hahn, 1991) is selected for time integration. According to this scheme, the system response is calculated as

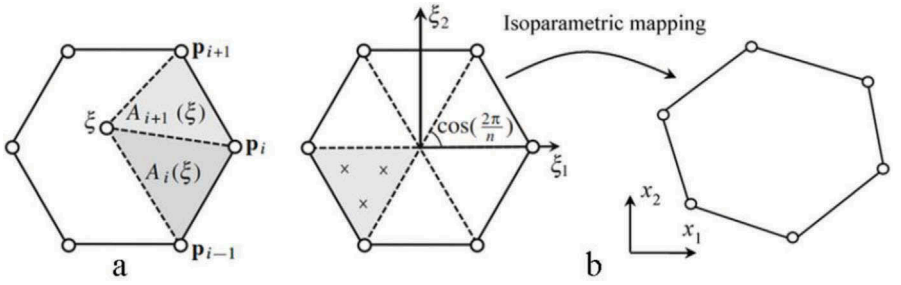

Figure 1. Illustration of the triangular areas used in the definition of Wachspress shape function (a), and the triangulation of the reference regular polygon with 3 integration points in each triangle, and the isoparametric mapping to a physical element (b).

$$\mathbf{M}\ddot{\mathbf{u}}_t + \mathbf{A}_{e=1}^{Nel}\mathbf{f}_t^{\text{int},e}(\boldsymbol{\sigma}) = \mathbf{f}_t^{\text{ext}} \text{with } \mathbf{f}_t^{\text{int},e} = \int_{\Omega^e} \mathbf{B}_e^{\text{T}}\boldsymbol{\sigma} d\Omega^e$$
$$\dot{\mathbf{u}}_{t+\Delta t} = \dot{\mathbf{u}}_t + \Delta t\ddot{\mathbf{u}}_t, \quad \mathbf{u}_{t+\Delta t} = \mathbf{u}_t + \Delta t\dot{\mathbf{u}}_{t+\Delta t} \tag{5}$$

where is the global nodal displacement vector, Δt is the time step, $\mathbf{f}_t^{\text{ext}}$ is the global external force vector, $\mathbf{f}_t^{\text{int},e}$ is the internal force vector for a finite element e, $\mathbf{B}_e$ is the kinematic operator, $\mathbf{A}$ is the assembly operator, and, finally, $\mathbf{M}$ is the lumped mass matrix obtained by the row summing technique.

3 NUMERICAL EXAMPLES

3.1 *Model geometry, mesh, boundary conditions and the material parameters*

The material properties and model parameters used in the simulations are as follows: Young's modulus E = 70 GPa, Poisson's ratio ν = 0.2, density ρ = 2600 kg/m^3, σ_{c0} = 200 MPa, σ_{t0} = 11 MPa, φ = 50°, ψ = 5°, G_{Ic} = 50 J/m^2, G_{IIc} = 5000 J/m^2, s_R = s_{MC} = 0.05 MPas. These values correspond to a hard rock like granite. Moreover, the rock is assumed homogeneous and without any initial faults for simplicity. The loading rate effects are not considered in this paper. Therefore, the viscosity moduli values are set relatively small so that they do not cause significant strain rate hardening effects at the strain rates occurring in the simulations here, see Saksala (2018) where these values did not result in observable strain rate hardening at a loading rate of 5 s^{-1} neither in compression nor in tension. However, viscosity in general has a stabilizing effect on numerical simulations.

The boundary conditions and the polygon mesh are shown in Figure 2.

The shape and dimensions of the tunnel as well as the seismic disturbance are the same as in the study by Li et al. (2018). This magnitude, 50 MPa, of the stress wave corresponds to the maximum particle velocity of 10 m/s.

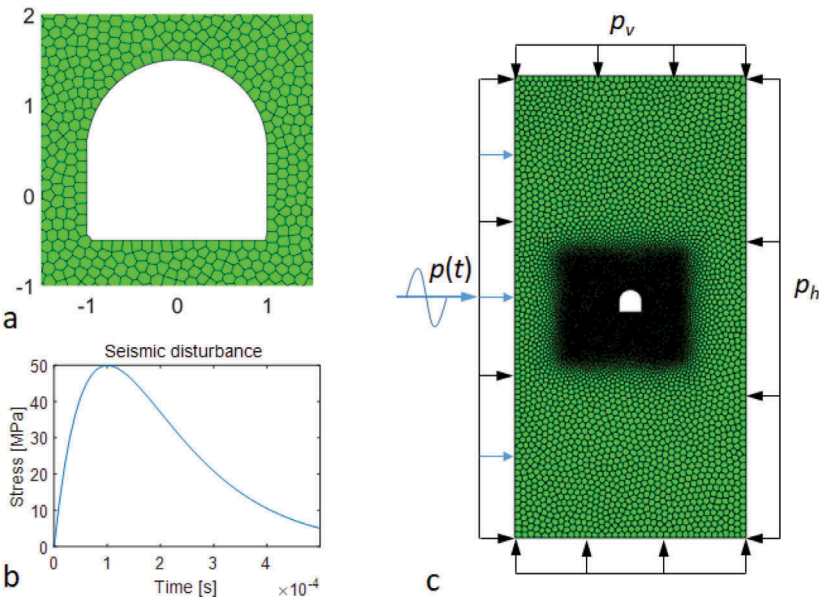

Figure 2. A detail of the mesh around the tunnel (the dimensions in [m]) (a), the seismic disturbance (b), the polygonal mesh with 10000 polygons and the boundary conditions (c).

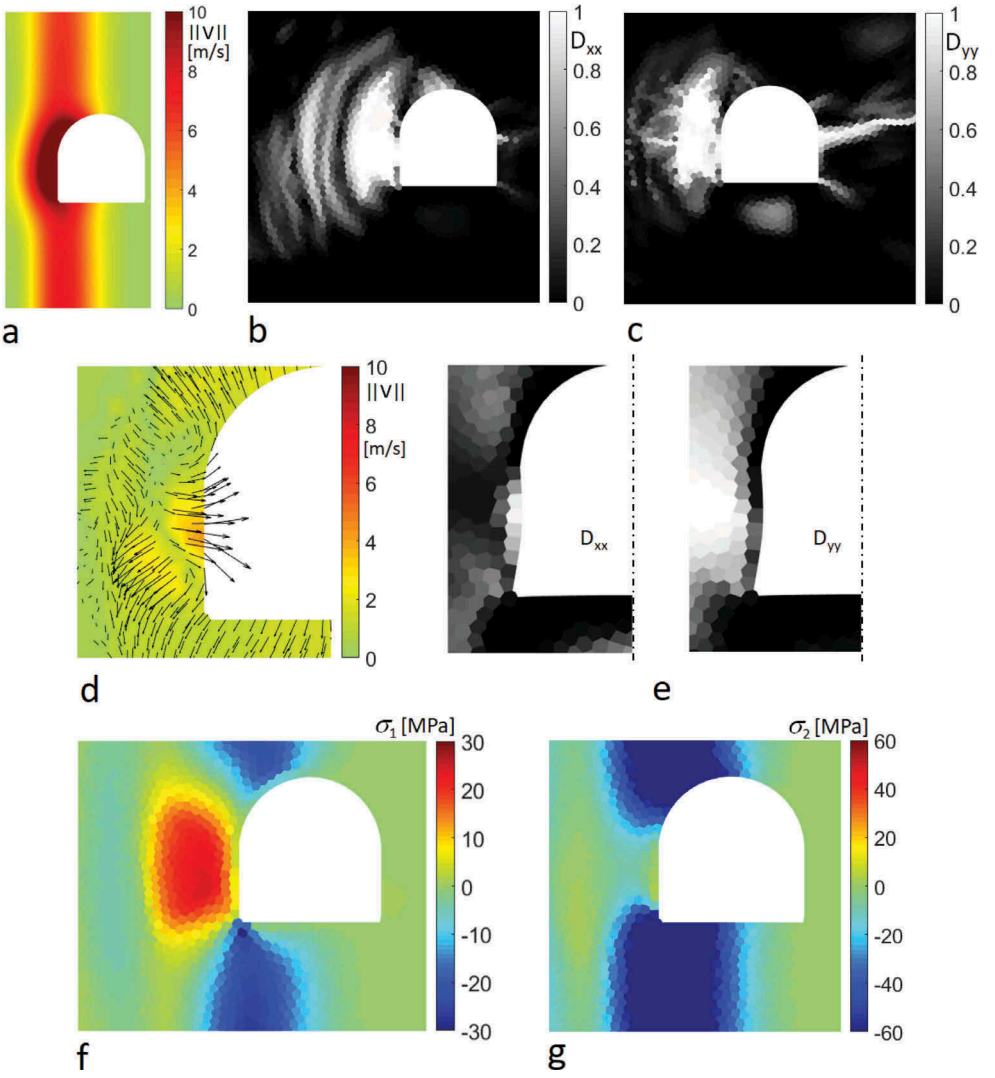

Figure 3. Simulation results for unconfined case: velocity magnitude at t = 1.9 ms (a), damage components D_{xx} (b) and D_{yy} (c) at t = 3.7 ms, the velocity magnitude plot with arrows indicating the direction and relative magnitude of nodal velocities at t = 2.5 ms (d), the damage components in the deformed mesh (magnification = 20) at the same time station (e), major (f) and minor (g) principal stresses at t = 1.9 ms.

3.2 *Unconfined case*

If the tunnel is close to the surface, there is neither significant overburden pressure nor horizontal pressure. This case is simulated first. The simulation results at few representative time stations are presented in Figure 2. It is not very illustrative to plot the components of the compliance tensor **D**. Instead of this, the damage parameters for plots are calculated as $D_{ii} = 1 - E_{d,ii}/E_{0,ii}$ where $E_{d,ii}$ and $E_{0,ii}$ are the diagonal entries of damaged and intact stiffness tensor, respectively. These behave as the classical scalar damage variable being 0 for intact rock and 1 for fully damaged rock. Moreover, it should be mentioned that compressive (shear) failures by the MC viscoplasticity model (2) above are not activated at the stress levels occurring in the present simulations.

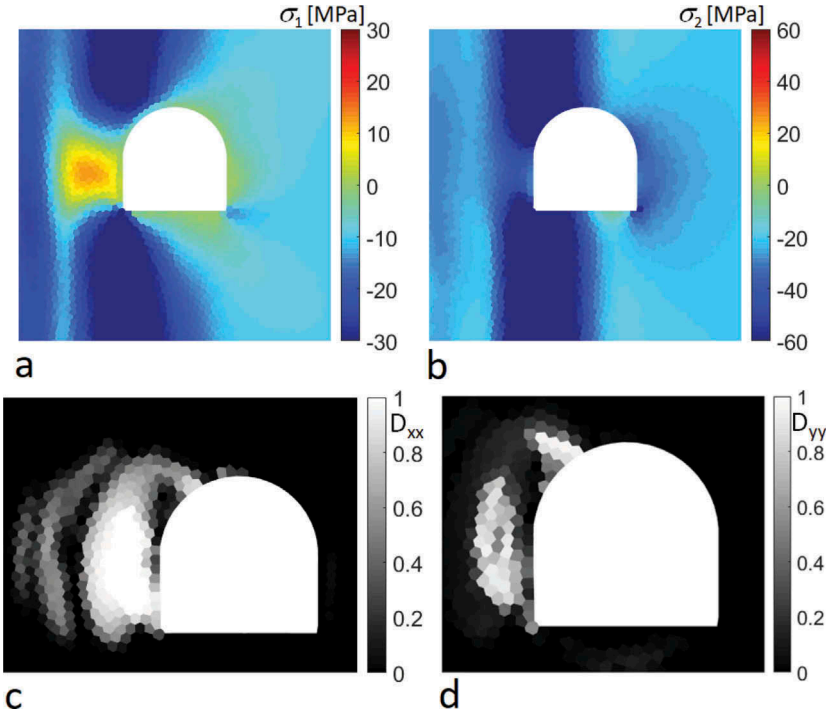

Figure 4. Simulation results with p_v = 20 MPa and p_h = 10 MPa: Major (a) and minor (b) principal stresses at t = 1.9 ms, and damage components D_{xx} (c) and D_{yy} (d) at t = 3.7 ms.

According to the results in Figure 3, rockburst takes place at the left wall of the tunnel due to the stress wave reflection. This is indicated in the damage component plots in Figure 3e and in Figure 3d where the velocity arrows in an area at the left surface of the tunnel point to the tunnel interior. This means that the material is ejected into the tunnel. The damage component plot at a later stage in Figure 3b and c show that the rock on the left side of the tunnel is severely damaged. Moreover, a large horizontal crack has initiated at the right wall of the tunnel and propagated some 2 meters to the right, as attested in the D_{yy} component plot in Figure 3c. Finally, the major and minor principal stresses plotted at t = 1.9 ms in Figure 3f and g demonstrate the reflection of the compressive stress wave at the left wall of the tunnel.

3.3 *Tunnel under overburden and horizontal pressure*

When a tunnel is excavated deep down in the bedrock, it is subjected to static overburden vertical and lateral pressures. Here, a simulation of a tunnel in such conditions with p_v = 20 MPa and p_h = 10 MPa (see Figure 2c) is carried out using the same seismic disturbance as in the unconfined case. The simulation results are shown in Figure 4.

In the confined case, the vertical overburden pressure suppresses considerably the rock failure reflected in the D_{yy} plot in Figure 4d. In contrast, the amount of damage in x-direction has not diminished as much (see Figure 4c). Indeed, the rock is still severely damaged at the area where the stress wave reflection takes place. Higher horizontal pressures would suppress the damage in horizontal direction more but, on the other hand, at high depths the walls of the tunnels become susceptible to a static failure. In any case, it can be observed that the present approach can predict a rockburst in an underground tunnel under *in-situ* stresses. Finally, it is noted that these simulation results are in qualitative agreement with those by Li et al. (2018) obtained by the particle based numerical manifold method.

4 CONCLUSIONS

A numerical method including an anisotropic visodamage-viscoplasticity model for rock implemented with the polygonal finite elements scheme was presented for modelling an underground tunnel under a seismic disturbance. The simulations demonstrated that the model could predict the rockburst, i.e. the ejection of crushed rock into the tunnel, induced by the seismic disturbance in terms of damage component plots and velocity quiver plots. Naturally, the present approach, due to the underlying continuum assumption, is inferior to discrete element methods in modelling rock crushing but superior in computational efficiency. Finally, this method should be further developed to include a method to account for the natural discontinuities in the rock mass. At the scale of an underground tunnel for cars for example, rock cannot be adequately assumed homogeneous and flawless.

ACKNOWLEDGEMENTS

This research was funded by Academy of Finland (Grant number 298345).

REFERENCES

Brady B.H.G., Brown, E.T. 1993. Rock mechanics for underground mining. Berlin: Springer.

Li, C.C. 2017. Principles of rockbolting design. Journal of Rock Mechanics and Geotechnical Engineering. 9(3):396-414.

Li, X., Li, X-F., Zhang, Q-B., Zhao, J. 2018. A numerical study of spalling and related rockburst under dynamic disturbance using a particle-based numerical manifold method (PNMM). Tunneling and Underground Space Technology 61:438-449.

Raffaldi, M.J., Loken, M.C. 2016. Framework for Simulating Fracture, Ejection, and Restraint of Rock around aMine Drift Subjected to Seismic Loading. Paper ARMA 16-0394 presented in 50th U.S. Rock Mechanics/Geomechanics Symposium, Houston, Texas, USA, 26-29 June 2016.

Saksala, T. 2018. Numerical modelling of rock fracture with a Hoek-Brown viscoplastic-damage model implemented with polygonal finite elements. In: Litvinenko, V. (ed.) Proceedings of the 2018 European Rock Mechanics Symposium (EUROCK2018: Geomechanics and Geodynamics of Rock Masses), Saint Petersburg, Russia, 22-26 May, 2018. Vol1, pp. 903-908.

Saksala, T. 2018. Combined Anisotropic Viscodamage-Viscoplasticity Model for Rock Under Dynamic Loading. In: Gdoutos, E. (ed.) Proceedings of the First International Conference on Theoretical, Applied and Experimental Mechanics(ICTAEM 2018), Paphos, Cyprus, June 17-20, 2018, Structural Integrity, vol 5. Springer.

Sukumar, N., Tabarraei, A. 2004. Conforming polygonal finite elements. International Journal for Numerical Methods in Engineering 61:2045-2066.

Talischi, C., Paulino, G.H., Pereira, A., Menezes, I.F.M. 2012. PolyMesher: a general-purpose mesh generator for polygonal elements written in Matlab. Structural and Multidisciplinary Optimization 45:309-328.

Talischi, C., Paulino, G.H., Pereira, A., Menezes, I.F.M. 2012. Poly Top: a Matlab implementation of a general topology optimization framework using unstructured polygonal finite element meshes. Structural and Multidisciplinary Optimization 45:329-357.

Wang, W.M., Sluys, L.J., De Borst, R. 1997. Viscoplasticity for instabilities due to strain softening and strain-rate softening. International Journal for Numerical Methods in Engineering 40:3839-3864.

Wen, K. Shimada, H., Sasaoka, T., Zhang, Z. 2017. Numerical study of plastic response of urban underground rock tunnel subjected to earthquake. International Journal of Geo-Engineering, 8-28.

Zhang, Q.B., Zhao, J. 2014. A review of dynamic experimental techniques and mechanical behaviour of rock materials. Rock Mechanics and Rock Engineering 47:1411-1478.